Magnetism and Interlayer Bonding in Pores of Bernal-Stacked Hexagonal Boron Nitride

Journal:	*Physical Chemistry Chemical Physics*
Manuscript ID	CP-ART-06-2022-002624.R1
Article Type:	Paper
Date Submitted by the Author:	26-Jul-2022
Complete List of Authors:	Dogan, Mehmet; UC Berkeley, Cohen, Marvin; UC Berkeley

SCHOLARONE™
Manuscripts

Magnetism and Interlayer Bonding in Pores of Bernal-Stacked Hexagonal Boron Nitride

Mehmet Dogan[1,2] and Marvin L. Cohen[1,2]
[1] *Department of Physics, University of California, Berkeley, California 94720, USA*
[2] *Materials Sciences Division, Lawrence Berkeley National Laboratory, Berkeley, California 94720, USA*

When single-layer *h*-BN is subjected to a high-energy electron beam, triangular pores with nitrogen edges are formed. Because of the broken sp^2 bonds, these pores are known to possess magnetic states. We report on the magnetism and electronic structure of triangular pores as a function of their size. Moreover, in the Bernal-stacked *h*-BN (AB-*h*-BN), multilayer pores with parallel edges can be created, which is not possible in the commonly fabricated multilayer AA′-*h*-BN. Given that these pores can be manufactured in a well-controlled fashion using an electron beam, it is important to understand the interactions of pores in neighboring layers. We find that in certain configurations, the edges of the neighboring pores remain open and retain their magnetism, and in others, they form interlayer bonds. We present a comprehensive report on these configurations for small nanopores. We find that at low temperatures, these pores have near degenerate magnetic configurations, and may be utilized in magnetoresistance and spintronics applications. In the process of forming larger multilayer nanopores, interlayer bonds can form, reducing the magnetization. Yet, unbonded parallel multilayer edges remain available at all sizes. Understanding these pores is also helpful in a multitude of applications such as DNA sequencing and quantum emission.

I. INTRODUCTION

Low-dimensional materials enable a wide range of uses not possible with bulk (three-dimensional) materials. Creating holes in two-dimensional (2D) materials, in particular, allows for applications like molecular sieving, metamaterials, and quantum emission [1–6]. Researchers can tailor a system for a specific application by controlling the size, shape, and/or distribution of holes in a 2D material. DNA sequencing using nanopores (holes as small as a few nm) is one example of such an application, which would allow for quick and precise sequencing of single unbroken DNA strands [7–11]. Nanopores also spontaneously form in 2D materials, so, understanding their properties is important in itself. In this study, we investigate the properties of triangular pores in single-layer hexagonal boron nitride (*h*-BN) and their interactions with pores in neighboring layers, which is largely determined by the stacking sequence and pore alignment. We focus primarily on Bernal-stacked *h*-BN which can house parallel-edged triangular pores in neighboring layers because of the lack of rotation between the layers [12].

Layers of *h*-BN can be stacked in different ways, resulting in different material properties [13–16]. The AA stacking [Figure 1(a)] is a trivial stacking sequence with no in-plane shift or rotation between successive layers, and it has an interlayer distance of 3.64 Å. We include this unobserved high-energy stacking sequence in our study as a reference. The most commonly synthesized stacking sequence of *h*-BN is the AA′ stacking [Figure 1(b)], in which each layer is a 60° rotated copy of the preceding layer, resulting in columns of alternating B and N atoms in the bulk [17]. A less common stacking sequence of *h*-BN is the AB (Bernal) stacking, which includes no relative rotation but only a relative shift between the layers [Figure 1(c,d)]. AB-*h*-BN is energetically very close to AA′-*h*-BN [16], but until recently, it was only observed in rare cases [18–20]. The procedure to reliably manufacture this stacking was recently reported [16], followed by several new studies on this material [21–24]. For a comprehensive comparison of the stacking sequences in *h*-BN, we refer the reader to Ref. [16].

An infinite sheet of single-layer *h*-BN is a wide-gap insulator, yet, computational investigations have revealed that its edges and pores have a diverse set of electronic and magnetic properties [12, 21, 25–29]. The unpaired electrons that occupy dangling sp^2 hybrid orbitals at edges and pores result in magnetism which is absent in the pristine sheet. The most commonly formed vacancies in *h*-BN are boron monovacancies (i.e. a single boron atom removed from the sheet), shown in Figure 2. These vacancies can be created by a high-energy electron beam in a transmission electron microscopy (TEM) chamber. As the beam is applied for longer periods of time, the vacancies grow into larger pores in predictable ways [16, 21, 30–32]. Although, in principle, many different pore geometries are possible, the pores that grow via electron beam have three nitrogen-terminated zigzag edges that form an equilateral triangle. In the large pore limit, these edges approximate the edges of an infinite sheet (N-edge), which is the most common edge type in *h*-BN [17, 33–39], and has magnetic properties that we elucidated in a previous computational study [12]. In the current study, we first investigate the spin configurations of nanopores of various sizes in single-layer *h*-BN and relate them to the infinite edges. We then discuss the interactions of nested/aligned pores in multilayer *h*-BN. In the common AA′-*h*-BN, consecutive layers are rotated by 60° with respect to each other, and triangular pores do not neatly align. In contrast, multilayer nested pores

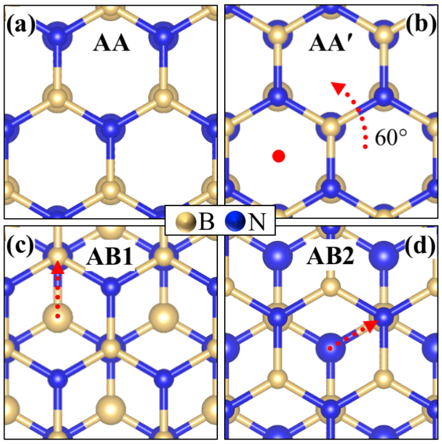

Figure 1. Four high-symmetry stacking sequences of h-BN considered in this study. (a) The AA stacking sequence which has not been observed experimentally. (b) The commonly observed AA′ stacking sequence, obtained from the AA stacking by a 60° rotation of the top layer around a hollow site center, marked in red. (c) The first way of constructing the AB stacking sequence (AB1) of h-BN. (d) The second way of constructing the AB stacking sequence (AB2) of h-BN. The two stacking sequences in (c,d) are physically equivalent but geometrically distinct once a top layer and a bottom layer are defined. They are distinguished so that the top and the bottom layers can be treated separately in this work. The atoms in the bottom layer are enlarged to ease inspection.

are observed in AB-h-BN with perfectly parallel edges [16, 21]. We report the geometries and electronic structures of all basic bilayer triangular pore combinations in which the larger of the two pores is 4 u.c. in size, and generalize the bonding patterns (or lack thereof) when available.

We conclude this section by noting that in AB-h-BN, the two consecutive layers are inequivalent. With the same bottom layer, the top layer may be shifted in two distinct ways to construct the AB stacking, shown in Figure 1(c,d) by the red arrows, which we call AB1 and AB2. This property of AB-h-BN clearly distinguishes it from AA′-h-BN and was recently utilized to generate ferroelectricity in bilayer h-BN [22–24]. In order to keep track of all nanopore combinations, we distinguish between AB1 and AB2 stackings for the rest of the study. Treating these two stackings separately allows us to study pore combinations only where the top pore is larger than or equal in size to the bottom pore, without missing or double-counting any nested pores. Assuming that the electron beam is applied from the top, this also corresponds to the experimental conditions and observations [16, 21, 32]. Therefore, we present a view of these nanopore systems that would correspond to the view of the experimentalist who is performing a TEM (or similar) measurement "from the top". For a more detailed discussion of this point, we refer the reader to Ref. [12].

II. METHODS

We conduct density functional theory (DFT) calculations within the Perdew–Burke–Ernzerhof generalized gradient approximation (PBE GGA) [40], using the QUANTUM ESPRESSO software package with norm-conserving pseudopotentials [41, 42]. The plane-wave energy cutoff for the pseudo Kohn-Sham wavefunctions used is 80 Ry. For a 1×1 unit cell of h-BN, we use a $12 \times 12 \times 1$ Monkhorst–Pack k-point mesh to sample the Brillouin zone [43], and choose k-point meshes accordingly for larger unit cells. A $\sim$14 Å of vacuum is placed between the copies of the 2D system along the out-of-plane direction to isolate the sheets. In order to include the interlayer van der Waals interactions, we include a Grimme-type dispersion correction [44]. All atomic coordinates are relaxed until the forces on all the atoms are less than 10^{-3} Ry$/a_0$ in all three Cartesian directions, where a_0 is the Bohr radius.

III. RESULTS

A. Nanopores in monolayer *h*-BN

We start with a survey of the possible spin configurations in the boron monovacancy in the single layer h-BN. Throughout this article, we label pores as "NTn", where "NT" stands for "nitrogen-terminated", and n is the number of nitrogen atoms on each edge of the triangle. Thus, a boron monovacancy is denoted as NT1. In Figure 2(a-d), we present the atomic structure of NT1 in its various magnetic configurations. Figure 2(a) is obtained by running a collinear calculation, resulting in a structure with 3-fold symmetry. The structures in Figure 2(b-d) are obtained by relaxing the atoms further with noncollinear (NC) spin channels and different starting configurations. All three of these configurations have lower energies compared to the collinear structure, as listed in Table I, and are local minima in the configuration space. We find that the 3-fold symmetric NC(30,150,270) structure has the lowest energy, but only by $\sim$ 2 meV, compared to NC(90,90,270). Interestingly, the latter configuration is a triplet of atomic structures, where there are two shorter N–N distances (2.70 Å) and a longer N–N distance (2.78 Å). At regular temperatures (20 K $< T <$ 500 K), we expect both the NC(30,150,270) and NC(90,90,270) pores to be present in single layer h-BN with pores with only trace amounts of NC(90,90,90). To the best of our knowledge, previous studies have only identified NC(90,90,90) [21, 45–47]. Although no probing of the local magnetism of edges or pores in h-BN has been reported, ferromagnetism has been shown to occur in h-BN at room temperature [48], which can be attributed to the existence of edges and pores in regular h-BN samples.

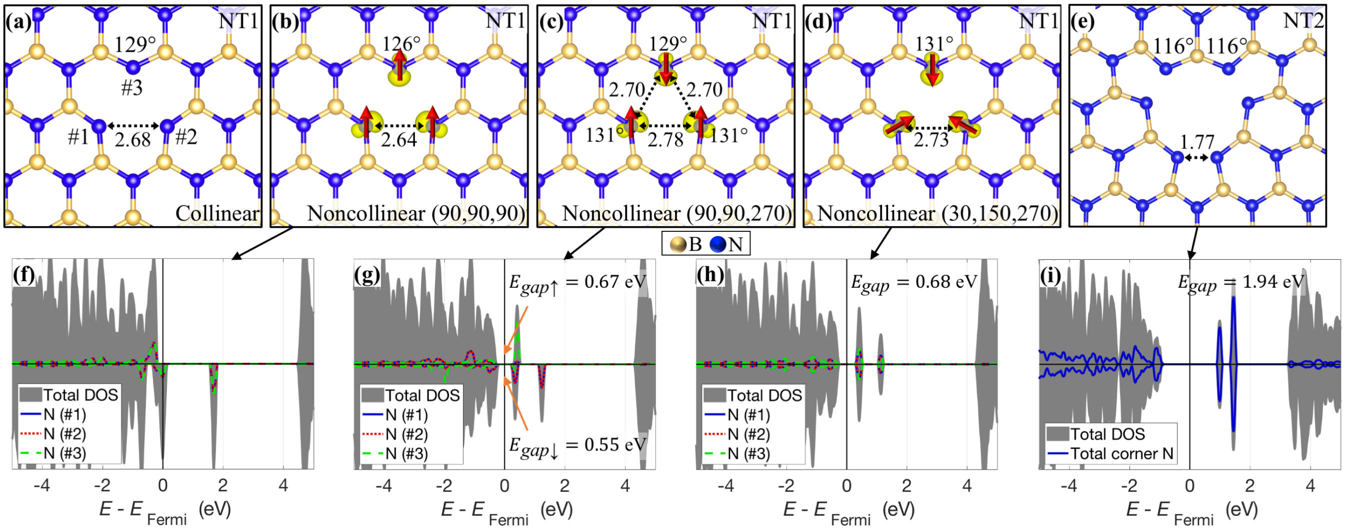

Figure 2. Atomic structures of the collinear (a) and noncollinear (b–d) spin configurations in the nitrogen-terminated pore with 1 nitrogen per edge (NT1); atomic structure of the nitrogen-terminated pore with 2 nitrogens per edge (NT2); spin-resolved projected densities-of-states (PDOS) plots for the noncollinear NT1 pores (f–h); PDOS plot for the NT2 pore (i). The isosurface plots for absolute magnetization with the isovalue $|n_\uparrow - n_\downarrow| = 0.02 \ |e|/a_0^3$ are included in the atomic structure pictures. The direction of magnetization on each magnetized atom is denoted by a red arrow, and the structures are labeled by these directions at the bottom right corner of panels (b–d). The magnetization directions are measured in degrees from the zigzag direction. The atoms on whose orbitals the densities-of-states are projected are labeled in (a). The Fermi energy is set to the mid-gap in cases where there is a band gap.

	NT1 (3)				NT2 (0)
	Collinear	NC(90, 90, 90)	NC(90, 90, 270)	NC(30, 150, 270)	Collinear
ΔE (eV)	$\equiv 0$	-0.138	-0.185	-0.187	$\equiv 0$
ES type	metal	half-metal	magnetic SC	nonmagnetic SC	nonmagnetic SC
$E_{gap\uparrow}$ (eV)	0	4.64	0.67	0.68	1.94
$E_{gap\downarrow}$ (eV)	0	0	0.55	0.68	1.94

Table I. Total energies (ΔE), electronic structure (ES) types and band gaps of the NT1 and NT2 nanopores. Refer to the text for the explanation of the labels in the second row. The total energies are with reference to the collinear configuration and presented per edge N atom, for instance, ΔE of and NT1 configuration is computed by subtracting the energy of the collinear configuration from it and dividing by 3 (the number of edge N atoms). "SC" stands for "semiconductor".

The next smallest triangular pore is NT2, which is obtained by removing three borons and one nitrogen from the system (Figure 2(e)). In this pore, the corner nitrogens approach each other and form dimers, resulting in a collinear electronic structure ($|n_\uparrow - n_\downarrow| = 0$ everywhere), as reported previously [21, 46].

Looking at the electronic structures of the NT1 pores (Figure 2(f-h)), we observe that the NC(90,90,90) pore is a half-metal, i.e. the majority spin channel is insulating and the minority spin channel is a metal, the NC(90,90,270) pore is a magnetic semiconductor and the NC(30,150,270) pore is a nonmagnetic semiconductor, although the electronic structures of the latter two configurations are very similar. The antiferromagnetic state is a semiconductor with a gap of 0.51 eV. Because the spin configuration and the electronic structure are closely linked, these pores may be useful in various spintronics applications [49–56]. As seen in Figure 2(i), the electronic structure of the NT2 pore is a nonmagnetic semiconductor with a larger gap (Table I). We present the atomic and electronic structures of larger pores in single layer *h*-BN (NT3–NT8) in Figures S1–S6. The key information for these larger pores is summarized in Table II. In each case, we fully relax the pore in a collinear calculation, and then run a self-consistent field calculation with two initial spin configurations: where all the edge spins are set as parallel (P), and where consecutive edge spins are set as antiparallel (AP). We note that we have confirmed in a few test cases that in these larger pores, further relaxations with noncollinearity cause negligible changes in atomic positions. In Figures S1–S6, the magnetization in the real space is only plotted for the P configurations (the AP configurations have equivalent plots with alternating sign). In Table II, we also include the case of the N-edge taken from Ref. [12], which may be interpreted as the limiting case NT∞.

From the results in Figures S1–S6 and Table II, we make a few observations: (i) The corner N atoms remain dimerized in these larger pores and thus have no magnetic moment. This causes the sequence of the absolute value of the magnetic moments to be approximately $3\mu_\mathrm{B}$, 0, $3\mu_\mathrm{B}$, $6\mu_\mathrm{B}$,... for the NT1, NT2, NT3, NT4,... pores. (ii) For the NTn pores with $n \geq 2$, the energy differences between P and AP spin configurations is smaller compared to NT1 and the N-edge. The comparison with NT1 can be explained by the isolation provided by the dimerized corner N atoms. The comparison with the N-edge may be due to the fact that these pores are still small, and many of the edge N atoms lack nearest and next-nearest neighbors to interact with, as opposed to the infinite edges (we know that both nearest and next-nearest neighbor interactions are important for the spin dynamics in this system, cf. [12]). This near degeneracy of different spin configurations would be advantageous in applications that rely on magnetic switching. (iii) The P configurations are consistently half-metals, and the AP configurations are either magnetic semiconductors (MSC) or nonmagnetic semiconductors (NMSC), depending on the number of available magnetic sites (written in parentheses in the first row of Table I and the first column of Table II). The band gap of the NMSC configurations gradually increases with the pore size, approaching the value of the N-edge (0.51 eV). (iv) The positions of the in-gap states for the AP configurations depend on the pore size. Because the pore size can be controlled by the duration of the applied electron beam [31, 32], it should be possible to engineer the desired in-gap states at a desired location on the h-BN layer.

		ΔE (eV)	ES type	$E_{gap(\uparrow,\downarrow)}$ (eV)
NT3 (3)	P	-0.230	half-metal	$0.41, 0$
	AP	-0.229	MSC	$0.15, 0.09$
NT4 (6)	P	-0.235	half-metal	$0.46, 0$
	AP	-0.242	NMSC	$0.31, 0.31$
NT5 (9)	P	-0.220	half-metal	$0.58, 0$
	AP	-0.225	MSC	$0.18, 0.29$
NT6 (12)	P	-0.225	half-metal	$0.70, 0$
	AP	-0.236	NMSC	$0.33, 0.33$
NT7 (15)	P	-0.226	half-metal	$0.72, 0$
	AP	-0.227	MSC	$0.25, 0.41$
NT8 (18)	P	-0.226	half-metal	$0.95, 0$
	AP	-0.229	NMSC	$0.36, 0.36$
N-edge [12]	P	-0.218	half-metal	$4.56, 0$
	AP	-0.184	NMSC	$0.51, 0.51$

Table II. Total energies (ΔE), electronic structure (ES) types and band gaps of the NT3–NT8 nanopores. Refer to the text for the explanation of P and AP labels. The total energies are with reference to the collinear configuration and presented per edge N atom, for instance, ΔE of an NT3 configuration is computed by subtracting the energy of the collinear configuration from it and dividing by 9 (the number of edge N atoms). The numbers in parentheses in the first column denote the number of magnetic N atoms for each pore. "(N)MSC" stands for "(non)magnetic semiconductor".

B. Nanopores in bilayer h-BN

When nanopores are created on multilayer h-BN, they tend to begin on the top layer and then propagate into the layers underneath [21, 32]. As a first step in understanding nanopores in multilayer systems, we present results on nanopores on the top layer of bilayer h-BN, where the bottom layer remains as a full sheet. In Figures S7–S22, we present the atomic and electronic structures of pores NT1–NT4 in a single sheet stacked on a full sheet using AA, AA$'$, AB1 and AB2 stacking sequences. For NT1, NT3 and NT4 pores, parallel (P) and antiparallel (AP) spin configurations are run without further relaxation of the atomic positions (NT2 remains fully spin-unpolarized), and the magnetization in the real space is only plotted for the P configurations (the AP configurations have equivalent plots with alternating sign). Our findings are also summarized in Table III. In general, the behavior of the pores in the bilayer remains very similar to their behavior in single h-BN sheets, although the small shifts in the energy levels. However, the magnetized regions around the edge N atoms do not lie entirely parallel to the sheet for the larger pores (NT3 and up), instead, these spin-polarized dangling orbitals point away from the bottom sheet by an angle θ, which is listed for each case in the table.

Once a nanopore begins to form in the top layer of multilayer h-BN, the second layer becomes exposed the electron beam, giving rise to progressively larger and deeper (in terms of the number of layers) pores [21, 32]. In

		AA			AA′			AB1			AB2		
		ΔE (eV)	$E_{gap(\uparrow,\downarrow)}$ (eV)	θ	ΔE	$E_{gap(\uparrow,\downarrow)}$	θ	ΔE	$E_{gap(\uparrow,\downarrow)}$	θ	ΔE	$E_{gap(\uparrow,\downarrow)}$	θ
NT1 (3)	P	-0.157	$4.08, 0$	0°	-0.164	$4.36, 0$	0°	-0.166	$4.48, 0$	0°	-0.161	$4.39, 0$	0°
	AP	-0.181	$0.29, 0.18$	0°	-0.203	$0.45, 0.34$	0°	-0.204	$0.40, 0.29$	0°	-0.212	$0.49, 0.38$	0°
NT2 (0)	Collinear	$\equiv 0$	1.75	n/a	$\equiv 0$	1.82	n/a	$\equiv 0$	1.71	n/a	$\equiv 0$	1.86	n/a
NT3 (3)	P	-0.224	$0.52, 0.23$	38°	-0.228	$0.51, 0$	34°	-0.231	$0.46, 0.20$	37°	-0.230	$0.59, 0.08$	35°
	AP	-0.215	$0.19, 0.17$	44°	-0.219	$0.06, 0$	16°	-0.227	$0.21, 0.20$	38°	-0.221	$0.07, 0$	36°
NT4 (6)	P	-0.232	$0.66, 0$	39°	-0.234	$0.66, 0$	39°	-0.238	$0.61, 0.09$	39°	-0.235	$0.58, 0.08$	37°
	AP	-0.215	$0.31, 0.31$	42°	-0.221	$0.22, 0.22$	6°	-0.226	$0.26, 0.26$	39°	-0.225	$0.29, 0.29$	5°

Table III. Total energies (ΔE), band gaps and tilt angles of the magnetized regions of the NT1–NT4 nanopores on the top sheet of *h*-BN bilayers. Refer to the text for the explanation of P and AP labels. The total energies are with reference to the collinear configuration and presented per edge N atom, for instance, ΔE of an NT3 configuration is computed by subtracting the energy of the collinear configuration from it and dividing by 9 (the number of edge N atoms). The numbers in parentheses in the first column denote the number of magnetic N atoms for each pore.

the next part of our work, we investigate the coexistence of small pores in both layers of bilayer *h*-BN in order to elucidate the early stages of this process. In Figures S23–S24, we present the NT1 pores on both layers of bilayer *h*-BN (in this case, AB2 stacking is identical to AB1 so it is not presented separately). The NT1 & NT1 configurations are uncoupled in the sense that the pores in the neighboring layers do not interact beyond the already present van der Waals forces. We note here that for the NT1 & NT1 configurations, we have checked for potential interlayer coupling of spins by running a comprehensive collection of spin polarization combinations. We have not found a noteworthy difference in energies beyond a simple summation of the energies of spin configurations in each layer.

As the next step in the process for the AB stacking, we remove the 3 N atoms of the bottom layer that are exposed in addition to the 1N atom on the top layer. This results in the configuration in Figure S25, which is an unusual defect structure where three B atoms in the bottom layer move inward within the plane and form a trimer. This magnetic semiconductor has the band gaps $(0.59, 0.43)$ eV in the two spin channels. We note that this structure is not an artifact of symmetry and seems to be robust with respect to atomic position perturbations.

For larger pores in bilayer *h*-BN, we focus on the AB stacking. As discussed above, due to the relative 60° rotation between consecutive layers in the AA′ stacking, multilayer pores become irregularly shaped, whereas the AB stacking allows for nested and aligned pores [21]. As the next step in AB1-*h*-BN, we assume that the NT2 pore has formed in the top layer, and then we remove the boron in the center of the exposed area in the bottom layer (cf. Figure S13). This results in the NT2 & NT1 structure presented in Figure S26, which is also a uncoupled structure (half-metal, $E_{gap\uparrow} = 1.95$ eV). Removing the 6 exposed nitrogens from this configuration results in our first coupled structure, presented in Figure 3(a). This 3-fold symmetric structure is a magnetic semiconductor which has 6 interlayer B–N bonds. Forming the NT2 & NT1 structure in AB2-*h*-BN is possible in two different ways by removing a boron from either the center or the corner of the exposed area in the bottom layer (cf. Figure S14). In both cases, we get uncoupled structures that are presented in Figures S27–S28 (both magnetic semiconductors with the band gaps $(0.46, 0.44)$ eV and $(0.49, 0.26)$ eV, respectively). Finally, we present the NT2 & NT2 structures in the AA and AB1 stacking sequences in Figures S29–S30, both of which are uncoupled and nonmagnetic semiconductors with the band gaps 1.53 eV and 1.74 eV, respectively (AB2 is equivalent to AB1).

We then move to the NT3 pore in the top layer of AB1-*h*-BN. Removing one of the three exposed borons in the bottom layer (cf. Figure S17) results in the NT3 & NT1 uncoupled structure (Figure S31), which is a half-metal with $E_{gap\uparrow} = 0.64$ eV. Similarly, the NT3 & NT2 structure in AB1-*h*-BN is also uncoupled (Figure S32) but metallic. Next, we remove the remaining exposed nitrogens so that all the atoms in the bottom layer that are exposed when the top layer has an NT3 pore are removed. This results in the structure in Figure 3(b) which has reflection symmetry and 9 interlayer B–N bonds, and is a magnetic semiconductor. An interesting effect occurs when the NT3 & NT3 structure in AB1-*h*-BN is set up and relaxed, in which two edge nitrogens in the bot-

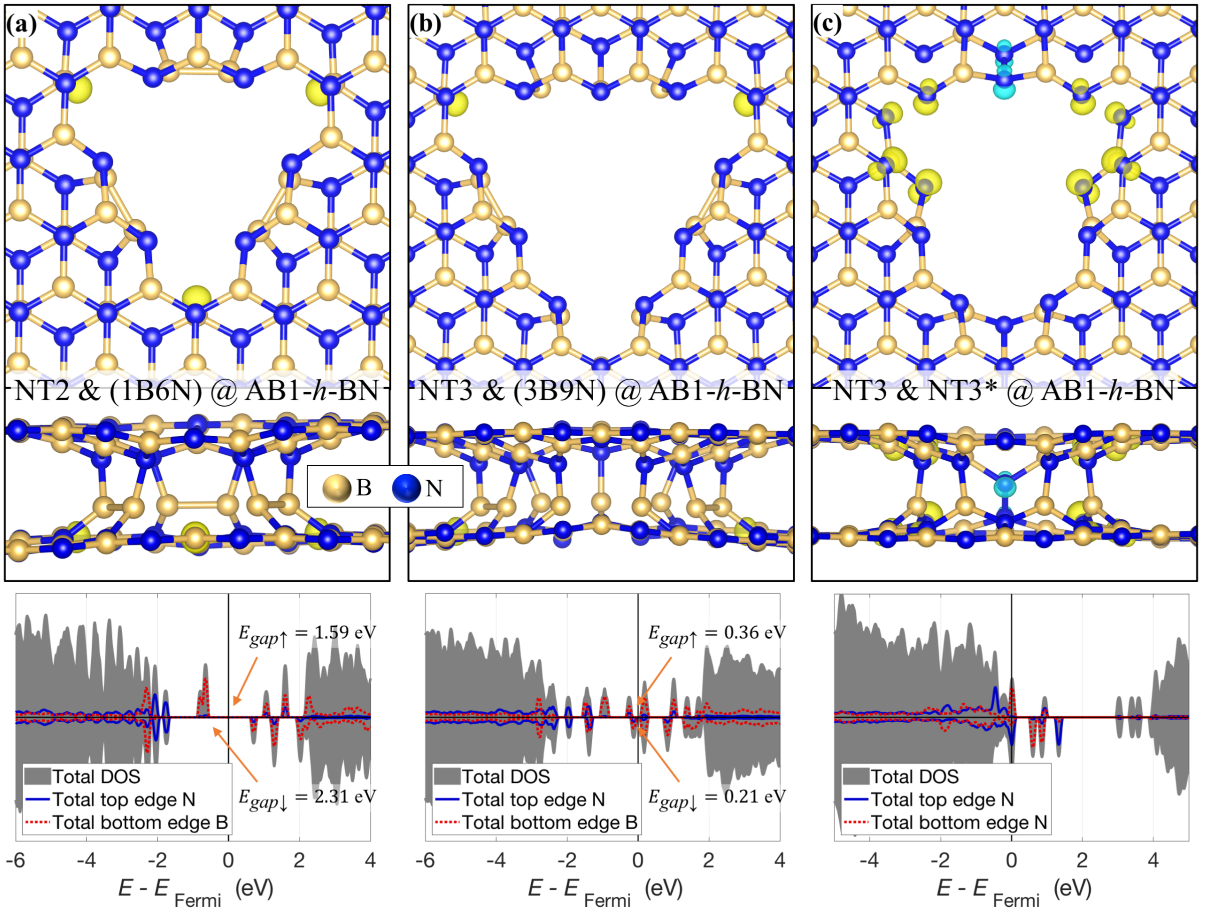

Figure 3. Atomic and electronic structures of bilayer pores in AB1-*h*-BN that result in coupled structures where the top layer is an NT2 or NT3 pore. (a) The NT2 & (1B6N) configuration. (b) The NT3 & (3B9N) configuration. (c) The NT3 & NT3* configuration. The isosurface plots for magnetization with the isovalue $n_{\uparrow} - n_{\downarrow} = \pm 0.02 \ |e|/a_0^3$ are included in the atomic structure pictures. Top view and side view of each nanopore are stacked vertically in each panel. For the spin-resolved density of states plots in the bottom row, the Fermi energy is set to the mid-gap in cases where there is a band gap.

tom layer detach from their neighbors and form an N_2 molecule. When the molecule is taken out of the system, the resulting coupled structure, which is metallic, is presented in Figure 3(c). Because the bottom layer has lost two nitrogens, we call this configuration NT3 & NT3*, and it has 4 interlayer B–N bonds as well as 1 interlayer N–N bond. This structure demonstrates that not all nested NTn_1 & NTn_2 pores are possible in their expected stoichiometry in bilayer and therefore multilayer AB-*h*-BN.

There are three inequivalent NT3 & NT1 structures in AB2-*h*-BN depending on which boron in the bottom layer is removed (cf. Figure S18). These three result in uncoupled half-metallic structures that are presented in Figures S33–S35 with $E_{gap\uparrow} = 0.63, 0.64, 0.66$ eV, respectively. The two inequivalent NT3 & NT2 structures in AB2-*h*-BN are also uncoupled and half-metallic, and presented in Figures S36–S37 ($E_{gap\uparrow} = 0.63, 0.61$ eV, respectively). The NT3 & NT3 structure in AB2-*h*-BN is equivalent to that in AB1-*h*-BN (Figure 3(c)). Finally, we present the NT3 & NT3 structure in the AA stacking sequence in Figure S38, which is a magnetic metal with interlayer bonding of the mid-edge nitrogens.

The largest size we have considered for bilayer *h*-BN in this study is the NT4 pore. We start with the NT4 & NT1 configuration in AB1-*h*-BN of which there are two (Figures S39–S40). Both of these are uncoupled and half-metallic with $E_{gap\uparrow} = 0.66, 0.69$ eV, respectively. When the bottom layer has an NT2 pore, interlayer bonds form, but not all the top edge nitrogens are bonded. This coupled configuration (NT4 & NT2) is presented in Figure S41 and is a half-metal with $E_{gap\uparrow} = 0.24$ eV. Enlarging the bottom layer pore one more step to set up the NT4 & NT3 structure results in the detachment of three N_2 molecules and 12 interlayer B–N bonds (Figure 4(a)). By losing most of its dangling orbitals, this system, which we call NT4 & NT3*, becomes a fairly large-gap magnetic semiconductor. Next, we remove the remaining exposed

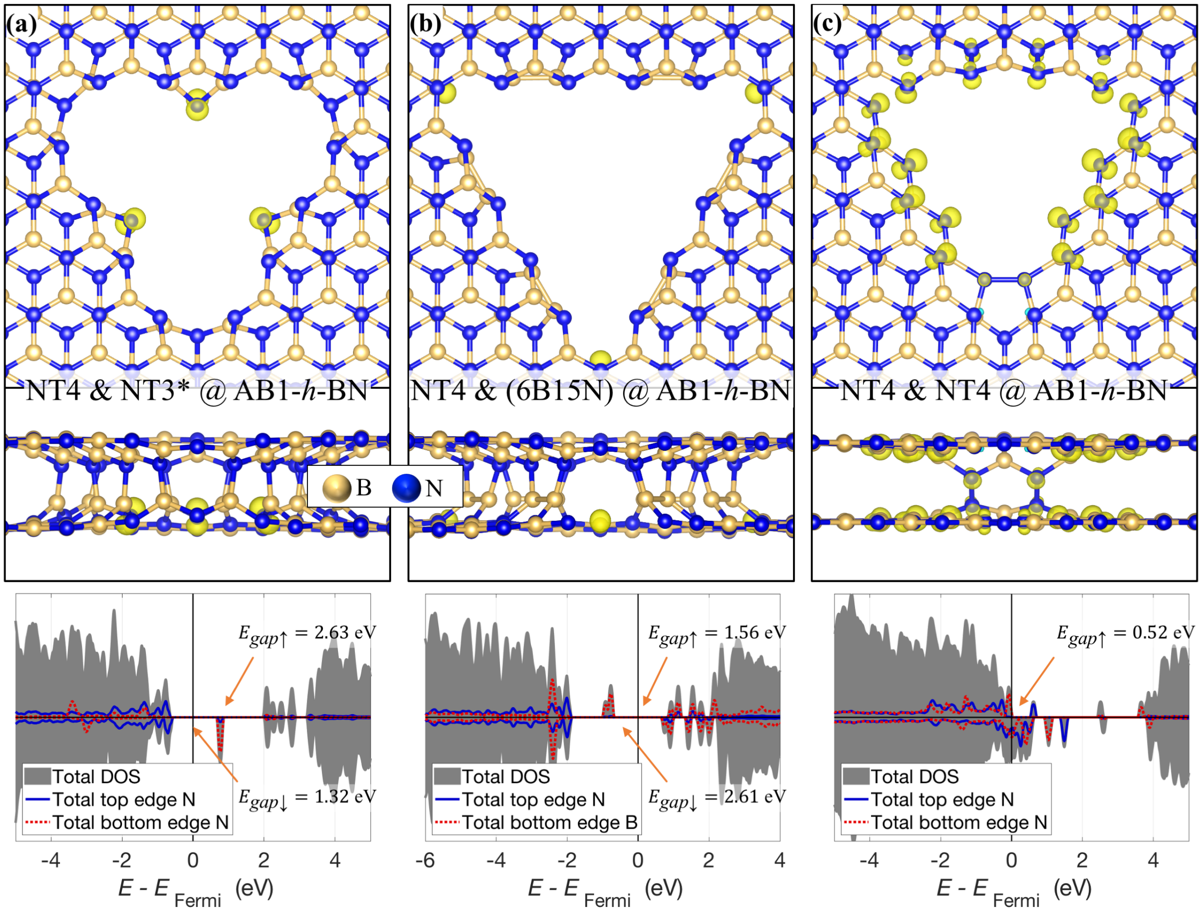

Figure 4. Atomic and electronic structures of bilayer pores in AB1-h-BN that result in coupled structures where the top layer is an NT4 pore. (a) The NT4 & NT3* configuration. (b) The NT4 & (6B15N) configuration. (c) The NT4 & NT4 configuration. The isosurface plots for magnetization with the isovalue $n_\uparrow - n_\downarrow = \pm 0.02\ \ |e|/a_0^3$ are included in the atomic structure pictures. Top view and side view of each nanopore are stacked vertically in each panel. For the spin-resolved density of states plots in the bottom row, the Fermi energy is set to the mid-gap in cases where there is a band gap.

nitrogens from this configuration so that all the atoms in the bottom layer that are exposed when the top layer has an NT4 pore are removed. This results in the structure in Figure 4(b) which has 12 interlayer B–N bonds and is a magnetic semiconductor. The NT4 & NT4 bilayer pore in AB1-h-BN also results in some interlayer bonding(Figure 4(c)). In this configuration, the alignment of the two edges (diagonal in Figure 4(b)) is different from the alignment of the remaining edge (horizontal in Figure 4(c). The interlayer bonds form only at the latter edge. These two edge types correspond to the infinite edges in Figures 5 and 6 of [12], respectively. This particular pattern of interlayer bonding should hold for all NTn & NTn pores ($n \geq 4$) of AB-h-BN, where $n - 2$ interlayer N–N bonds occur only at one of the edges.

In AB2-h-BN, there are four inequivalent NT4 & NT1 structures depending on which boron in the bottom layer is removed (cf. Figure S22). These structures are presented in Figures S42–S45. The NT4 & NT1 (1) structure has a single interlayer N–N bond and is a magnetic metal. The NT4 & NT1 (2) structure has two interlayer N–N bonds and is a magnetic half-metal with $E_{gap\uparrow} = 0.57$ eV. The remaining two NT4 & NT1 structures are uncoupled half-metals with $E_{gap\uparrow} = 0.48, 0.60$ eV, respectively. The three inequivalent NT4 & NT2 structures are presented in Figures S46–S48. These structures are uncoupled half-metals with $E_{gap\uparrow} = 0.57, 0.62, 0.63$ eV, respectively. Among the two inequivalent NT4 & NT3 configurations, the first one (Figure S49) has 2 interlayer N–N bonds and is a magnetic metal. This bonding pattern should hold for all NTn & NT$(n-1)$ pores ($n \geq 4$) of AB-h-BN, where $n-3$ interlayer N–N bonds each occur at two of the edges. The second NT4 & NT3 configuration in AB2-h-BN (Figure S50) is an uncoupled structure that is a half-metal with $E_{gap\uparrow} = 0.58$ eV. The NT4 & NT4 structure in AB2-h-BN is equivalent to that in AB1-h-BN (Figure 4(c)). Finally, the NT4 & NT4 structure in the AA stacking sequence is presented in Figure S51, which is a magnetic half-metal ($E_{gap\uparrow} = 2.78$ eV) with interlayer bonding of the two mid-edge nitrogens on each edge.

We close this section by commenting on pores in thicker (multilayer) AB-h-BN. Although, strictly speaking, deeper nested triangular pores need to be studied separately, the information derived from bilayer pores allows us to guess the configuration of a particular multilayer nested pore. In particular, for a given layer that has two neighbors, its interaction with each of its neighbors would be predicted based on our calculations. If both of its neighbors are expected to be uncoupled based on bilayer calculations, it would be expected to remain uncoupled. If only one of its neighbors is expected to form interlayer bonds, these bonds would be expected to form and not be affected by the uncoupled layer on the opposite side. If both of its neighbors are expected to form interlayer bonds with this layer, the resulting structure would be harder to predict; however, since nested pores are expected to form from top to bottom, the interlayer bonds with the layer above would have a better chance to form. This method allows us to generate plausible guesses for any given multilayer nested pore.

IV. CONCLUSION

We conducted a first-principles study of the nitrogen-terminated triangular nanopores in h-BN with a special focus on Bernal-stacked h-BN (AB-h-BN). We found that the ground state of the smallest pore (B monovacancy) is a 3-fold symmetric configuration with zero total magnetization. However, the existence of magnetic configurations that are almost degenerate with the ground state heightens the potential of magnetic switchability. For larger pores in single-layer h-BN, configurations with parallel and antiparallel neighboring magnetizations are also close in energy, indicating the likelihood of easier magnetization of these pores compared to longer edges where energy differences are larger. For bilayer configurations with pores in both layers, we find that in most cases, the layers remain uncoupled, *i.e.*, no significant out-of-plane movement or bonding occurs. However, several structures that are expected to occur during electron irradiation do form interlayer bonds, reducing the magnetic character of the pores. We expect these types of coupled structures to occur during electron irradiation alongside the simpler decoupled structures. We also find that some nested pores are not possible in their expected stoichiometry in bilayer and therefore multilayer AB-h-BN as a result of to the detachment of nitrogens by forming N_2 molecules. We expect these findings to inform future investigations into the pores of thicker multilayer AB-h-BN as well. We hope that our results will motivate experimental studies that closely investigate the magnetic and electronic properties of these pores in h-BN, given their enormous potential in applications such as DNA sequencing.

ACKNOWLEDGMENTS

This work was supported by the Director, Office of Science, Office of Basic Energy Sciences, Materials Sciences and Engineering Division, of the U.S. Department of Energy under contract No. DE-AC02-05-CH11231, within the Theory of Materials program (KC2301), which supported first-principles computations of the atomic structures. Further support for theoretical work was provided by the NSF Grant No. DMR-1926004 which supported first-principles computations of the precise electronic structures. Computational resources used were Cori at National Energy Research Scientific Computing Center (NERSC), which is supported by the Office of Science of the US Department of Energy under contract no. DE-AC02-05-CH11231, Stampede2 at the Texas Advanced Computing Center (TACC) through Extreme Science and Engineering Discovery Environment (XSEDE), which is supported by National Science Foundation (NSF) under grant no. ACI-1053575, Frontera at TACC, which is supported by NSF grant no. OAC-1818253, and Bridges-2 at the Pittsburgh Supercomputing Center (PSC), which is supported by NSF award number ACI-1928147.

[1] Koenig SP, Wang L, Pellegrino J, Bunch JS. Selective molecular sieving through porous graphene. Nature Nanotechnology. 2012 Nov;7(11):728–732. Available from: https://www.nature.com/articles/nnano.2012.162.

[2] Choi S, Tran TT, Elbadawi C, Lobo C, Wang X, Juodkazis S, et al. Engineering and Localization of Quantum Emitters in Large Hexagonal Boron Nitride Layers. ACS Applied Materials & Interfaces. 2016 Nov;8(43):29642–29648. Available from: https://doi.org/10.1021/acsami.6b09875.

[3] Zhao J, He G, Huang S, Villalobos LF, Dakhchoune M, Bassas H, et al. Etching gas-sieving nanopores in single-layer graphene with an angstrom precision for high-performance gas mixture separation. Science Advances. 2019 Jan;5(1):eaav1851. Available from: https://advances.sciencemag.org/content/5/1/eaav1851.

[4] Caldwell JD, Aharonovich I, Cassabois G, Edgar JH, Gil B, Basov DN. Photonics with hexagonal boron nitride. Nature Reviews Materials. 2019 Aug;4(8):552–567. Number: 8 Publisher: Nature Publishing Group. Available from: https://www.nature.com/articles/s41578-019-0124-1.

[5] Liu H, You CY, Li J, Galligan PR, You J, Liu Z, et al. Synthesis of hexagonal boron nitrides by chemical vapor deposition and their use as single photon emitters. Nano Materials Science. 2021 Sep;3(3):291–312. Available from: https://www.sciencedirect.com/science/article/pii/S2589965121000131.

[6] Song SB, Yoon S, Kim SY, Yang S, Seo SY, Cha S, et al. Deep-ultraviolet electroluminescence and photocurrent generation in graphene/hBN/graphene heterostructures. Nature Communications. 2021 Dec;12(1):7134. Number: 1 Publisher: Nature Publishing Group. Available from: https://www.nature.com/articles/s41467-021-27524-w.

[7] Liu S, Lu B, Zhao Q, Li J, Gao T, Chen Y, et al. Boron Nitride Nanopores: Highly Sensitive DNA Single-Molecule Detectors. Advanced Materials. 2013;25(33):4549–4554. Available from: https://onlinelibrary.wiley.com/doi/abs/10.1002/adma.201301336.

[8] Zhou Z, Hu Y, Wang H, Xu Z, Wang W, Bai X, et al. DNA Translocation through Hydrophilic Nanopore in Hexagonal Boron Nitride. Scientific Reports. 2013 Nov;3:3287. Available from: https://www.nature.com/articles/srep03287.

[9] Muthukumar M, Plesa C, Dekker C. Single-molecule sensing with nanopores. Physics Today. 2015 Aug;68(8):40–46. Publisher: American Institute of Physics. Available from: https://physicstoday.scitation.org/doi/10.1063/PT.3.2881.

[10] Heerema SJ, Dekker C. Graphene nanodevices for DNA sequencing. Nature Nanotechnology. 2016 Feb;11(2):127–136. Available from: https://www.nature.com/articles/nnano.2015.307.

[11] Deamer D, Akeson M, Branton D. Three decades of nanopore sequencing. Nature Biotechnology. 2016 May;34(5):518–524. Available from: https://www.nature.com/articles/nbt.3423.

[12] Dogan M, Cohen ML. Magnetic multilayer edges in Bernal-stacked hexagonal boron nitride. Physical Review B. 2020 Oct;102(15):155419. Publisher: American Physical Society. Available from: https://link.aps.org/doi/10.1103/PhysRevB.102.155419.

[13] Qi Y, Hector LG. Planar stacking effect on elastic stability of hexagonal boron nitride. Applied Physics Letters. 2007 Feb;90(8):081922. Available from: https://aip.scitation.org/doi/10.1063/1.2679007.

[14] Marom N, Bernstein J, Garel J, Tkatchenko A, Joselevich E, Kronik L, et al. Stacking and Registry Effects in Layered Materials: The Case of Hexagonal Boron Nitride. Physical Review Letters. 2010 Jul;105(4):046801. Available from: https://link.aps.org/doi/10.1103/PhysRevLett.105.046801.

[15] Constantinescu G, Kuc A, Heine T. Stacking in Bulk and Bilayer Hexagonal Boron Nitride. Physical Review Letters. 2013 Jul;111(3):036104. Available from: https://link.aps.org/doi/10.1103/PhysRevLett.111.036104.

[16] Gilbert SM, Pham T, Dogan M, Oh S, Shevitski B, Schumm G, et al. Alternative stacking sequences in hexagonal boron nitride. 2D Materials. 2019 Mar;6(2):021006. Available from: https://iopscience.iop.org/article/10.1088/2053-1583/ab0e24.

[17] Alem N, Erni R, Kisielowski C, Rossell MD, Gannett W, Zettl A. Atomically thin hexagonal boron nitride probed by ultrahigh-resolution transmission electron microscopy. Physical Review B. 2009 Oct;80(15):155425. Available from: https://link.aps.org/doi/10.1103/PhysRevB.80.155425.

[18] Warner JH, Rümmeli MH, Bachmatiuk A, Büchner B. Atomic Resolution Imaging and Topography of Boron Nitride Sheets Produced by Chemical Exfoliation. ACS Nano. 2010 Mar;4(3):1299–1304. Available from: https://doi.org/10.1021/nn901648q.

[19] Khan MH, Casillas G, Mitchell DRG, Liu HK, Jiang L, Huang Z. Carbon- and crack-free growth of hexagonal boron nitride nanosheets and their uncommon stacking order. Nanoscale. 2016 Sep;8(35):15926–15933. Available from: https://pubs.rsc.org/en/content/articlelanding/2016/nr/c6nr04734c.

[20] Ji Y, Calderon B, Han Y, Cueva P, Jungwirth NR, Alsalman HA, et al. Chemical Vapor Deposition Growth of Large Single-Crystal Mono-, Bi-, Tri-Layer Hexagonal Boron Nitride and Their Interlayer Stacking. ACS Nano. 2017 Dec;11(12):12057–12066. Available from: https://doi.org/10.1021/acsnano.7b04841.

[21] Dogan M, Gilbert SM, Pham T, Shevitski B, Ercius P, Aloni S, et al. Electron beam-induced nanopores in Bernal-stacked hexagonal boron nitride. Applied Physics Letters. 2020 Jul;117(2):023102. Publisher: AIP Publishing LLC AIP Publishing. Available from: https://aip.scitation.org/doi/abs/10.1063/5.0010891.

[22] Yasuda K, Wang X, Watanabe K, Taniguchi T, Jarillo-Herrero P. Stacking-engineered ferroelectricity in bilayer boron nitride. Science. 2021 Jun;372(6549):1458–1462. Publisher: American Association for the Advancement of Science Section: Report. Available from: https://science.sciencemag.org/content/372/6549/1458.

[23] Stern MV, Waschitz Y, Cao W, Nevo I, Watanabe K, Taniguchi T, et al. Interfacial ferroelectricity by van der Waals sliding. Science. 2021 Jun;372(6549):1462–1466. Publisher: American Association for the Advancement of Science Section: Report. Available from: https://science.sciencemag.org/content/372/6549/1462.

[24] Woods CR, Ares P, Nevison-Andrews H, Holwill MJ, Fabregas R, Guinea F, et al. Charge-polarized interfacial superlattices in marginally twisted hexagonal boron nitride. Nature Communications. 2021 Jan;12(1):347. Available from: https://www.nature.com/articles/s41467-020-20667-2.

[25] Barone V, Peralta JE. Magnetic Boron Nitride Nanoribbons with Tunable Electronic Properties. Nano Letters. 2008 Aug;8(8):2210–2214. Available from: https://doi.org/10.1021/nl080745j.

[26] Lai L, Lu J, Wang L, Luo G, Zhou J, Qin R, et al. Magnetic Properties of Fully Bare and Half-Bare Boron Nitride Nanoribbons. The Journal of Physical Chemistry C. 2009 Feb;113(6):2273–2276. Available from: https://doi.org/10.1021/jp8079827.

[27] Mukherjee R, Bhowmick S. Edge Stabilities of Hexagonal Boron Nitride Nanoribbons: A First-Principles Study. Journal of Chemical Theory and Computation. 2011 Mar;7(3):720–724. Available from: https://doi.org/10.1021/ct1006345.

[28] Yamijala SS, Pati SK. Electronic and Magnetic Properties of Zigzag Boron-Nitride Nanoribbons with Even and Odd-Line Stone-Wales (5–7 Pair) Defects. The Journal of Physical Chemistry C. 2013 Feb;117(7):3580–3594. Available from: https://doi.org/10.1021/jp310614u.

[29] Deng J, Yin Y, Niu H, Ding X, Sun J, Medhekar NV. The Edge Stresses and Phase Transitions for Magnetic BN Zigzag Nanoribbons. Scientific Reports. 2017 Aug;7(1):7855. Available from: https://www.nature.com/articles/s41598-017-08364-5.

[30] Alem N, Erni R, Kisielowski C, Rossell MD, Hartel P, Jiang B, et al. Vacancy growth and migra-

tion dynamics in atomically thin hexagonal boron nitride under electron beam irradiation. Physica Status Solidi – Rapid Research Letters. 2011 Aug;5(8):295–297. Available from: https://onlinelibrary.wiley.com/doi/abs/10.1002/pssr.201105262.

[31] Pham T, Gibb AL, Li Z, Gilbert SM, Song C, Louie SG, et al. Formation and Dynamics of Electron-Irradiation-Induced Defects in Hexagonal Boron Nitride at Elevated Temperatures. Nano Letters. 2016 Nov;16(11):7142–7147. Available from: https://doi.org/10.1021/acs.nanolett.6b03442.

[32] Gilbert SM, Dunn G, Azizi A, Pham T, Shevitski B, Dimitrov E, et al. Fabrication of Subnanometer-Precision Nanopores in Hexagonal Boron Nitride. Scientific Reports. 2017 Nov;7(1):15096. Available from: https://www.nature.com/articles/s41598-017-12684-x.

[33] Zobelli A, Gloter A, Ewels CP, Seifert G, Colliex C. Electron knock-on cross section of carbon and boron nitride nanotubes. Physical Review B. 2007 Jun;75(24):245402. Available from: https://link.aps.org/doi/10.1103/PhysRevB.75.245402.

[34] Meyer JC, Chuvilin A, Algara-Siller G, Biskupek J, Kaiser U. Selective Sputtering and Atomic Resolution Imaging of Atomically Thin Boron Nitride Membranes. Nano Letters. 2009 Jul;9(7):2683–2689. Available from: https://doi.org/10.1021/nl9011497.

[35] Kotakoski J, Jin CH, Lehtinen O, Suenaga K, Krasheninnikov AV. Electron knock-on damage in hexagonal boron nitride monolayers. Physical Review B. 2010 Sep;82(11):113404. Available from: https://link.aps.org/doi/10.1103/PhysRevB.82.113404.

[36] Kim JS, Borisenko KB, Nicolosi V, Kirkland AI. Controlled Radiation Damage and Edge Structures in Boron Nitride Membranes. ACS Nano. 2011 May;5(5):3977–3986. Publisher: American Chemical Society. Available from: https://doi.org/10.1021/nn2005443.

[37] Ryu GH, Park HJ, Ryou J, Park J, Lee J, Kim G, et al. Atomic-scale dynamics of triangular hole growth in monolayer hexagonal boron nitride under electron irradiation. Nanoscale. 2015 Jun;7(24):10600–10605. Available from: https://pubs.rsc.org/en/content/articlelanding/2015/nr/c5nr01473e.

[38] Rajan AG, Silmore KS, Swett J, Robertson AW, Warner JH, Blankschtein D, et al. Addressing the isomer cataloguing problem for nanopores in two-dimensional materials. Nature Materials. 2019 Feb;18(2):129–135. Number: 2 Publisher: Nature Publishing Group. Available from: https://www.nature.com/articles/s41563-018-0258-3.

[39] Mouhoub O, Martinez-Gordillo R, Nelayah J, Wang G, Park JH, Kim KK, et al. Quantitative insights into the growth mechanisms of nanopores in hexagonal boron nitride. Physical Review Materials. 2020 Jan;4(1):014005. Publisher: American Physical Society. Available from: https://link.aps.org/doi/10.1103/PhysRevMaterials.4.014005.

[40] Perdew JP, Zunger A. Self-interaction correction to density-functional approximations for many-electron systems. Physical Review B. 1981 May;23(10):5048–5079. Available from: http://link.aps.org/doi/10.1103/PhysRevB.23.5048.

[41] Giannozzi P, Baroni S, Bonini N, Calandra M, Car R, Cavazzoni C, et al. QUANTUM ESPRESSO: a modular and open-source software project for quantum simulations of materials. Journal of Physics: Condensed Matter. 2009;21(39):395502. Available from: http://iopscience.iop.org/article/10.1088/0953-8984/21/39/395502.

[42] Hamann DR. Optimized norm-conserving Vanderbilt pseudopotentials. Physical Review B. 2013 Aug;88(8):085117. Available from: https://link.aps.org/doi/10.1103/PhysRevB.88.085117.

[43] Cohen ML, Schlüter M, Chelikowsky JR, Louie SG. Self-consistent pseudopotential method for localized configurations: Molecules. Physical Review B. 1975 Dec;12(12):5575–5579. Available from: https://link.aps.org/doi/10.1103/PhysRevB.12.5575.

[44] Grimme S. Semiempirical GGA-type density functional constructed with a long-range dispersion correction. Journal of Computational Chemistry. 2006 Nov;27(15):1787–1799. Available from: https://onlinelibrary.wiley.com/doi/abs/10.1002/jcc.20495.

[45] Si MS, Xue DS. Magnetic properties of vacancies in a graphitic boron nitride sheet by first-principles pseudopotential calculations. Physical Review B. 2007 May;75(19):193409. Available from: https://link.aps.org/doi/10.1103/PhysRevB.75.193409.

[46] Du A, Chen Y, Zhu Z, Amal R, Lu GQM, Smith SC. Dots versus Antidots: Computational Exploration of Structure, Magnetism, and Half-Metallicity in Boron-Nitride Nanostructures. Journal of the American Chemical Society. 2009 Dec;131(47):17354–17359. Available from: https://doi.org/10.1021/ja9071942.

[47] Zhao LS, Chen CP, Liu LL, Yu HX, Chen Y, Wang XC. Magnetism and piezoelectricity of hexagonal boron nitride with triangular vacancy. Chinese Physics B. 2018 Jan;27(1):016301. Available from: https://doi.org/10.1088%2F1674-1056%2F27%2F1%2F016301.

[48] Si MS, Gao D, Yang D, Peng Y, Zhang ZY, Xue D, et al. Intrinsic ferromagnetism in hexagonal boron nitride nanosheets. The Journal of Chemical Physics. 2014 May;140(20):204701. Available from: https://aip.scitation.org/doi/10.1063/1.4879055.

[49] Prinz GA. Magnetoelectronics. Science. 1998 Nov;282(5394):1660–1663. Publisher: American Association for the Advancement of Science Section: Review. Available from: https://science.sciencemag.org/content/282/5394/1660.

[50] Wolf SA, Awschalom DD, Buhrman RA, Daughton JM, Molnár Sv, Roukes ML, et al. Spintronics: A Spin-Based Electronics Vision for the Future. Science. 2001 Nov;294(5546):1488–1495. Publisher: American Association for the Advancement of Science Section: Special Reviews. Available from: https://science.sciencemag.org/content/294/5546/1488.

[51] Žutić I, Fabian J, Das Sarma S. Spintronics: Fundamentals and applications. Reviews of Modern Physics. 2004 Apr;76(2):323–410. Publisher: American Physical Society. Available from: https://link.aps.org/doi/10.1103/RevModPhys.76.323.

[52] Awschalom DD, Flatté ME. Challenges for semiconductor spintronics. Nature Physics. 2007 Mar;3(3):153–159. Number: 3 Publisher: Nature Publishing Group. Available from: https://www.nature.com/articles/nphys551.

[53] Felser C, Fecher GH, Balke B. Spintronics: A Challenge for Materials Science and Solid-State Chemistry. Ange-

wandte Chemie International Edition. 2007;46(5):668–699. Available from: https://onlinelibrary.wiley.com/doi/abs/10.1002/anie.200601815.

[54] Yazyev OV. Emergence of magnetism in graphene materials and nanostructures. Reports on Progress in Physics. 2010 Apr;73(5):056501. Publisher: IOP Publishing. Available from: https://doi.org/10.1088%2F0034-4885%2F73%2F5%2F056501.

[55] Awschalom DD, Bassett LC, Dzurak AS, Hu EL, Petta JR. Quantum Spintronics: Engineering and Manipulating Atom-Like Spins in Semiconductors. Science. 2013 Mar;339(6124):1174–1179. Publisher: American Association for the Advancement of Science Section: Review. Available from: https://science.sciencemag.org/content/339/6124/1174.

[56] Ahn EC. 2D materials for spintronic devices. npj 2D Materials and Applications. 2020 Jun;4(1):1–14. Number: 1 Publisher: Nature Publishing Group. Available from: https://www.nature.com/articles/s41699-020-0152-0.